ALMA as a Prominence Thermometer: First Observations

Petr Heinzel[1,2] , Arkadiusz Berlicki[2,3,1] , Miroslav Bárta[1] , Paweł Rudawy[3] , Stanislav Gunár[1] , Nicolas Labrosse[4] , and
Krzysztof Radziszewski[3]
[1] Astronomical Institute, The Czech Academy of Sciences, 25165 Ondřejov, Czech Republic; pheinzel@asu.cas.cz
[2] University of Wrocław, Center of Scientific Excellence—Solar and Stellar Activity, Kopernika 11, 51-622 Wrocław, Poland
[3] Astronomical Institute, University of Wrocław, Kopernika 11, 51-622 Wrocław, Poland
[4] SUPA, School of Physics and Astronomy, University of Glasgow, Glasgow G12 8QQ, UK

Abstract

We present first prominence observations obtained with Atacama Large Millimeter Array (ALMA) in Band 3 at the wavelength of 3 mm. High-resolution observations have been coaligned with the MSDP Hα data from Wrocław–Białków large coronagraph at similar spatial resolution. We analyze one particular cotemporal snapshot, first calibrating both ALMA and MSDP data and then demonstrating a reasonable correlation between both. In particular, we can see quite similar fine-structure patterns in both ALMA brightness-temperature maps and MSDP maps of Hα intensities. Using ALMA, we intend to derive the prominence kinetic temperatures. However, having current observations only in one band, we use an independent diagnostic constraint, which is the Hα line integrated intensity. We develop an inversion code and show that it can provide realistic temperatures for brighter parts of the prominence where one gets a unique solution, while within faint structures, such inversion is ill conditioned. In brighter parts, ALMA serves as a prominence thermometer, provided that the optical thickness in Band 3 is large enough. In order to find a relation between brightness and kinetic temperatures for a given observed Hα intensity, we constructed an extended grid of non-LTE prominence models covering a broad range of prominence parameters. We also show the effect of the plane-of-sky filling factor on our results.

Unified Astronomy Thesaurus concepts: Solar prominences (1519)

1. Introduction

Spectral diagnostics of the prominence plasmas has been carried out for decades and is continuously improving thanks to new high-resolution ground and space instruments and more and more sophisticated non-LTE (i.e., departures from local thermodynamic equilibrium) modeling techniques (Labrosse et al. 2010; Vial & Engvold 2015). However, based predominantly on the analysis of spectral-line intensities and shapes, it poses the difficult task of discriminating between various competing processes. Line intensity depends on kinetic temperature, but also on density, prominence illumination, and other factors, and only a set of suitably selected lines of different atomic species can provide well-constrained diagnostics. The thermal broadening of lines is also competing with nonthermal ones, namely with the so-called microturbulence. Several recent studies are based on multiline diagnostics, e.g., Park et al. (2013), Ruan et al. (2019), Okada et al. (2020), and Peat et al. (2021), but the temperature is always determined indirectly, sometimes using specific assumptions. However, we need to know the plasma kinetic temperature as precisely as possible in order to discriminate between various heating and cooling processes, which are still poorly understood (Gilbert 2015). One promising way to determine the temperature more directly is to use the continuum observations and namely those in the radio domain where the Rayleigh–Jeans limit greatly simplifies the analysis. This was already considered in the past (see a short review in Heinzel et al. 2015 and in Wedemeyer et al. 2016), but the Atacama Large

Millimeter Array (ALMA) only recently started to provide radio observations with much better spatial resolution, comparable with that in the optical domain. In order to predict the visibility of prominences in various ALMA spectral bands, Heinzel et al. (2015) used the Hα coronagraphic observations obtained at the Astronomical Observatory of the University of Wrocław in Bialków, Poland, and converted the optical images to ALMA ones. ALMA is often considered to be a plasma "thermometer"; however, as shown in Heinzel et al. (2015), the prominences and their fine structures are in most cases only moderately optically thick in ALMA radio bands, and thus, their brightness temperature is lower or much lower than the kinetic one. In order to determine the optical thickness, one can use the integrated Hα intensity, which correlates well with the plasma emission measure. Therefore, by developing a suitable technique, one can convert the brightness temperature into a realistic kinetic one using the integrated Hα intensity to constrain the optical thickness. The obvious advantage of continuum diagnostics is that it does not depend on plasma dynamics. We may also assume that the integrated intensity of the Hα line is only weakly sensitive to line broadening. Of course, that is not true for the shape of the Hα line profiles.

Motivated by our previous study (Heinzel et al. 2015), we have been proposing coordinated ALMA and Hα observations during several ALMA cycles in the frame of different teams. Finally, such observations took place on 2018 April 19—see Section 2. The advantage of these observations is that they are recorded almost simultaneously in the radio and Hα bands. These observations have been partially analyzed in the PhD thesis of A. Rodger (Rodger 2019) and further explored in Labrosse et al. (2022). In the present paper, we performed complex ALMA data processing and calibration using the extended experience of the European ALMA Regional Center

(ARC) at the Astronomical Institute of Czech Academy of Sciences in Ondřejov. We then coaligned our Hα observations with ALMA and developed an inversion technique to determine the prominence kinetic temperature. This technique is based on an extensive grid of non-LTE prominence models constructed specifically for this study.

2. ALMA Observation

We have analyzed observations of the prominence performed on 2018 April 19, in the frame of project 2017.0.01138.S (PI N. Labrosse). For the sake of direct comparison with the Hα data (see Section 3), we have chosen just a small subset of the collected data publicly available in the ALMA archive, namely, the execution blocks (EBs) uid-A002-Xcc3ae3-Xb15e—a small inter-ferometric (INT) mosaic (five pointings) in ALMA Band 3 (continuum at ≈3 mm, in the frequency ranges 93.0–97.0 GHz and 103.0–107.0 GHz) and the complementary total-power (TP) scan of the entire solar disk–uid-A002-Xcc3ae3-Xb1f5. These EBs are cotemporal with the Hα observations.

The INT data have been calibrated and imaged in CASA by the standard procedure described in Shimojo et al. (2017) and the TP data according to White et al. (2017). For the imaging of the INT measurement set, we have reduced our selection to the shortest possible time interval ≈37.5 s required for the full-mosaic scan between 15:38:07 and 15:38:44 UT. The reason for this short-timescale imaging is rooted in the prominence dynamics that can blur the image: Longer integrations exhibit visibly less fine structures. The INT and TP data have been subsequently combined by CASA task feather() in order to recover low-frequency Fourier components missing in the INT data. Beforehand, the necessary prerequisites have been performed: recalculation of the TP image to Jy beam^{-1}, its shift to the same reference frame as the INT one, cropping the relevant region in the TP data and regrid, removal of the primary-beam (PB) correction in the INT image, etc. We have also cropped both (INT + TP) images to the same size (a subimage of INT) in order to keep just the data with high-enough signal (removing the border where the PB gain is low). The feather() task takes care of the proper handling of the overlapping range of Fourier components of the TP and INT images. Eventually, the final combined image (brightness) has been rescaled from Jy beam^{-1} to Kelvin and the reference frame transformed from celestial R.A./decl. to the solar HPC as described in Skokić & Brajša (2019).

The INT/TP combination of the solar data has its caveats, especially for the limb observations. The disparity between the two signals, and from that the implied necessity to scale them properly, has been reported in Alissandrakis et al. (2017). The feather() task allows the INT and TP data to be matched by fitting two free parameters. We have used this option and scaled the data basically in line with the procedure of Alissandrakis et al. (2017) in such a way that the combined image (1) has the average brightness temperature in the quiet solar region selected farther from the limb corresponding to that obtained from the purely TP data, and (2) the average brightness temperature of the corona (i.e., the small off-limb region selected farther from the prominence) is approximately zero (specifically, that it is not significantly negative). For this reason, we have tried several values of the sdfactor parameters in the CASA feather() task. The best fit of the above two requirements is reached for a scaling factor of 0.8, which we have used in our combined image. Still,
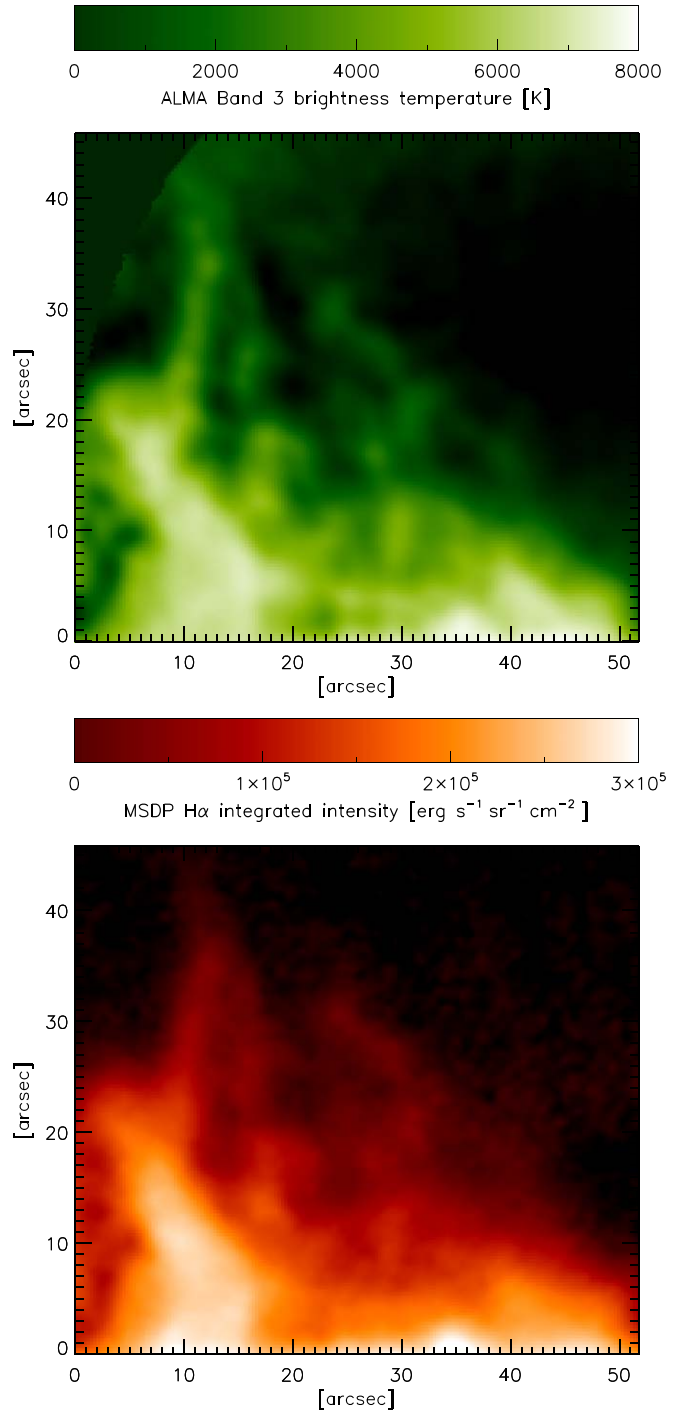

Figure 1. Coaligned maps of the brightness temperature T_b obtained from the calibrated ALMA Band 3 INT mosaic (top) and Hα integrated intensities from MSDP Wrocław/Bialków (bottom). The spatial resolution of both images is comparable, between $1''$ and $2''$. ALMA and MSDP data were recorded simultaneously, at 15:38:07 UT (start of the ALMA mosaic) and 15:37:56 UT (start of MSDP Hα scan). Individual fine structures are easily recognized in both images.

somewhat slightly negative values of T_b are present in the corona, showing an imperfectness in the total flux reconstruc-tion. However, significant distortions (a rim of under- and overshoots like in Shimojo et al. 2017) are not visible. The rotated and further cropped (with just the prominence region selected) brightness-temperature map obtained by the above-described procedure is displayed in Figure 1.

3. MSDP Hα Observations

The same prominence was also observed in the optical range above the southwest part of the solar limb (PA = 220°) with the Large Coronagraph (Gnevyshev et al. 1967; Rompolt & Rudawy 1985) equipped with the Multi-channel Subtractive Double Pass (MSDP) imaging spectrograph (Mein 1991; Rompolt 1994) at the Astronomical Observatory of the University of Wrocław in Bialków, Poland. The observations of the prominence started at 10:02:41 UT, finished at 15:54:46 UT, and were obtained in the scanning mode in the hydrogen Hα line. In total, 739 scans were recorded.

The Large Coronagraph (LC) is a classical Lyot-type instrument with a 53 cm diameter main objective and nearly 14.5 m effective focal length. The MSDP imaging spectrographs provide two-dimensional images over the Hα line profile (Mein 1977). The MSDP installed in Bialków has a nine-channel prism box. The prism box forms nine images of the same area on the Sun (called channels) but shifted by $\Delta\lambda = 0.4$ Å in wavelength between the consecutive channels. The range of wavelength bands of a single channel is $\Delta\lambda = 4.3$ Å.

For each scan, after the reduction procedure, we constructed a set of 23 narrowband nearly monochromatic images (wave band $\Delta\lambda = 0.06$ Å) of the whole field of view (FOV) (up to ±1.2 Å from the Hα line center), as well as the Hα line profile at each pixel in the FOV. The spatial resolution of the obtained images is limited by seeing, on average to about 1.5 arcsec. The data were calibrated to the absolute units of the specific intensity using the quiet-Sun reference spectrum. In addition, to obtain correct values of the prominence absolute intensities in each pixel, we removed the scattered light. That is particularly important for weak structures observed above the solar limb. Local intensities of the scattered light were evaluated for all observed altitudes above the solar limb, for all position angles within a segment of the ring with height and width larger than the observed prominence, and for all analyzed wavelengths using relevant data averaged over large structure-free regions located on both sides of the prominence.

From the whole set of data we chose the scan observed from 15:37:56 UT, 11 s before the time when the ALMA mosaic started to be reconstructed. The duration of the MSDP scan was 19 s. It is worth noticing that between 15:38:07 and 15:38:15 UT, the prominence was observed really simultaneously with ALMA and MSDP. In the next step, for this spectral image, using calibrated Hα line profiles for all pixels covering the prominence, we computed the Hα integrated intensities ($E(\text{H}\alpha)$) by integrating the line profiles within ±1 Å from the line center. These intensities, together with ALMA brightness temperatures T_b, are then used to determine the kinetic temperatures of the prominence plasma. The map of the prominence integrated intensities is shown in Figure 1.

4. Formation of ALMA Continua in Prominences

The radio continuum formation in prominences was reviewed in Heinzel et al. (2015) where the reader can find all necessary information. The dominant source of opacity is the hydrogen thermal free–free continuum having the absorption coefficient in the form

$$\kappa_\nu(\text{H}) = 3.7 \times 10^8 T^{-1/2} n_e n_p \nu^{-3} g_{ff}, \tag{1}$$

where n_e and n_p are the electron and proton densities, respectively, T is the kinetic temperature, ν is the frequency,

and g_{ff} is the Gaunt factor. In prominences, H⁻ free–free opacity can be ignored as estimated in Heinzel et al. (2015). Taking into account the correction for stimulated emission, one gets the expression often used in the literature:

$$\kappa_\nu = 0.018 n_e n_p T^{-3/2} \nu^{-2} g_{ff}. \tag{2}$$

The specific intensity I_ν for radiation normally emergent from the prominence on the limb is expressed as

$$I_\nu = \int B_\nu(T) e^{-t_\nu} dt_\nu, \tag{3}$$

where $B_\nu(T)$ is the Planck source function and t_ν the optical depth. Although the continuum source function is Planckian (for considered free–free processes), the spectrum formation is not governed by LTE conditions. Under characteristic prominence conditions, n_e and n_p depend on the non-LTE radiative transfer mainly in hydrogen and helium continua, where the photoionization and radiative recombination processes play a dominant role in the ionization equilibrium.

In the radio domain, I_ν and B_ν are directly proportional to the brightness temperature T_b and to the plasma kinetic temperature T_k, respectively,

$$I_\nu = \frac{2\nu^2 k}{c^2} T_b \quad B_\nu = \frac{2\nu^2 k}{c^2} T_k, \tag{4}$$

where c is the speed of light. Using this Rayleigh–Jeans law, Equation (3) can be written as

$$T_b = \int T_k e^{-t_\nu} dt_\nu. \tag{5}$$

Assuming a uniform kinetic temperature T_k along the line of sight (LoS), we have for a prominence slab of total optical thickness τ_ν

$$T_b = f \, T_k (1 - e^{-\tau_\nu}), \tag{6}$$

where $\tau_\nu = \kappa_\nu L$ and L is the effective geometrical thickness of the prominence. f is the plane-of-sky (PoS) filling factor to account for lower spatial resolution (e.g., Irimajiri et al. 1995). In the optically-thin limit, we get simply $T_b = f T_k \tau(\nu)$. At low spatial resolution, we always obtain a lower-limit estimate for T_k if the filling factor is ignored (i.e., set to unity); see also our results below.

As we see from the above relations, the brightness temperature of the prominence at a given position and a given frequency thus depends on the kinetic temperature, filling factor, and optical thickness. The latter is directly proportional to the emission measure EM $= n_e^2 L$, provided that $n_e = n_p$, which applies to a pure hydrogen plasma.

5. Prominence Kinetic Temperatures

5.1. Forward Modeling

Our primary goal is to determine the prominence kinetic temperature independently of the shapes of spectral lines, which are often distorted by microturbulence and other plasma dynamics. ALMA should provide ideal means for that because the radio continuum emission is not affected by dynamics. Moreover, knowing the optical thickness at a given frequency, we can directly relate the brightness to kinetic temperatures as described above. Observing the prominence simultaneously in at least two ALMA bands (frequencies) where the continuum

opacity substantially differs, one can get the kinetic temperature and optical thickness (e.g., Bastian et al. 1993; Rodger & Labrosse (2017); Gunár et al. 2018). However, in our present case, we only have ALMA Band 3 coverage of the prominence, and thus, we have to use some additional constraints. Assuming that the continuum optical thickness is proportional to the total emission measure (EM) along the LoS EM, we can use a robust correlation between such EM and integrated Hα line intensity $E(H\alpha)$. This correlation is only weakly dependent on kinetic temperature as demonstrated by Gouttebroze et al. (1993). For a given measured $E(H\alpha)$ we get slightly different EMs depending on the kinetic temperature. We use an extended grid of 1D slab prominence models with fine steps of 100 K in kinetic temperatures (see below for a more detailed description of these models) to search for the best fit between observed and synthetic $E(H\alpha)$ for each temperature separately. The step of 100 K is quite reasonable owing to calibration inaccuracies of Hα. In this way, we get the EM for each temperature bin and from that, we can compute the continuum optical thickness and then the brightness temperature T_b. We did this forward modeling for a few characteristic plasma temperatures and for the range of $E(H\alpha)$ as found in MSDP data. In Figure 2(a) we plot all prominence pixels, together with the synthetic T_b computed under the assumption that the whole prominence has a uniform kinetic temperature. This statistical analysis shows several interesting features. First, we find a good correlation between ALMA T_b and MSDP $E(H\alpha)$, apart from some scatter, which indicates that both ALMA and MSDP observations were reasonably well calibrated. Second, by plotting the synthetic curves of T_b versus $E(H\alpha)$, we see that for $E(H\alpha) \geqslant 10^5$ erg cm^{-2} s^{-1} sr^{-1} (hereafter these units are referred to as cgs) the brightness temperature increases with increasing T_{kin}, and we can see that the best fit of the latter is between 6000 and 7000 K. On the other hand, for pixels with $E(H\alpha) \leqslant 10^5$ cgs, the synthetic T_b is almost the same for all considered T_{kin}. In this range the optical thickness in Band 3 is small and thus the relation between T_b and T_k is rather ill conditioned, meaning that we cannot determine the kinetic temperature with reasonable accuracy. The last interesting observation is that all pixels are located below the color-coded curves, which may look strange at first sight. However, this indicates that the location of the data points is not determined primarily by the data scatter. We interpret such behavior as due to the ALMA PoS filling factor f lower than one. In Equation (6), the r.h.s. is multiplied by f and then the actual T_b is lower than in the case of $f = 1$ for which the color-coded curves were synthesized. Interestingly, for $E(H\alpha) \leqslant 10^5$ cgs, one could estimate the value of f as just the ratio of observed and color-coded T_b, simply because the latter is almost insensitive to T_{kin} in the considered range. However, this cannot be done for $E(H\alpha) \geqslant 10^5$ cgs, where T_b splits according to T_k, the property that allows us to determine the kinetic temperature by inversions. In such a case, we have to assume a certain value of f as discussed below. Note that at the largest $E(H\alpha)$, T_b saturates to T_k as expected and under such conditions, ALMA can be considered as a direct thermometer.

5.2. Inversions

In Heinzel et al. (2015), we proposed the temperature diagnostics using one selected ALMA band and simultaneous Hα observations. However, in the course of the present investigation, we realized that such a method can work only for bright parts of prominences while for weaker parts, the
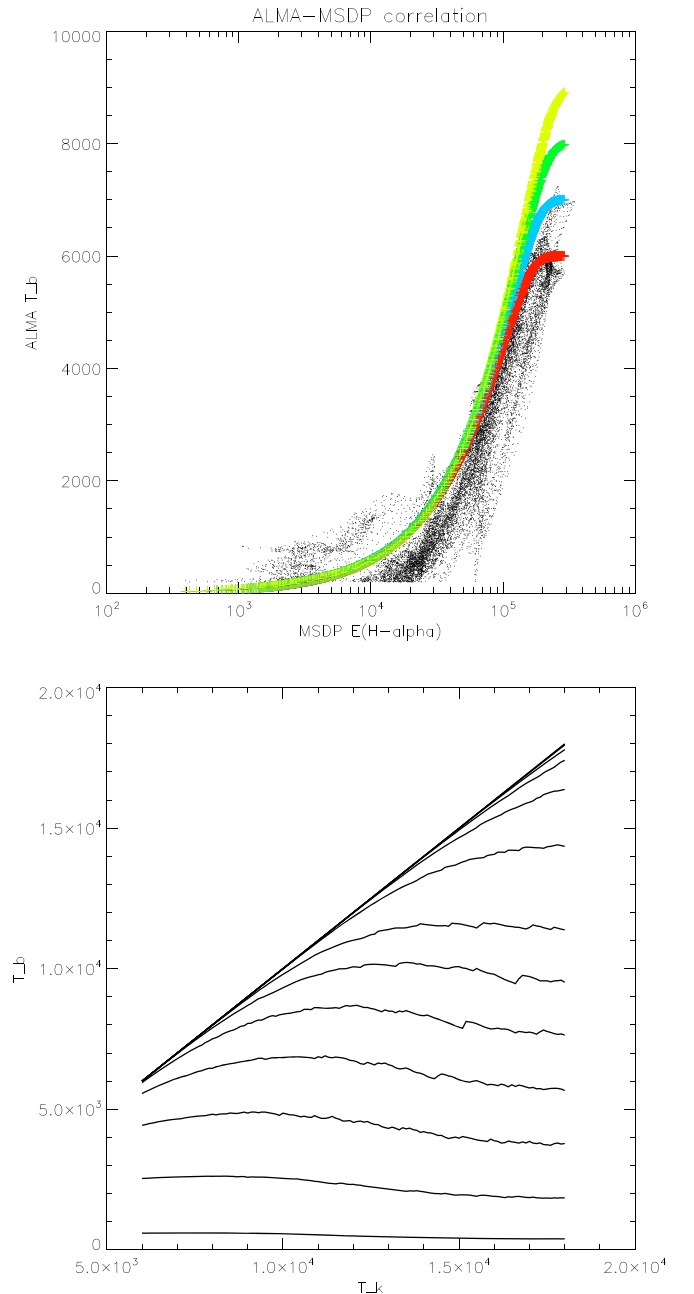

Figure 2. (a) Relation between observed T_b and $E(H\alpha)$ for all pixels from Figure 1 (dots). Colored curves indicate the same relation constructed from our models and assuming a uniform distribution of kinetic temperatures in the whole FOV (yellow—9000 K, green—8000 K, blue—7000 K, red—6000 K). Note that by multiplying each color curve by a certain value of f, one can see the effect of the filling factor. (b) Theoretical variations of the Band 3 brightness temperature T_b vs. 1D slab kinetic temperature T_k for several values of the Hα line integrated intensity. This plot was constructed from the grid of models (the small kinks on some curves are due to the finite separation between the models in the grid). The individual curves correspond (from below) to $E(H\alpha)$ from 10^4 up to 10^6 erg cm^{-2} s^{-1} sr^{-1}; the third curve from the bottom is for our limiting value 10^5.

inversion problem is ill conditioned. This is demonstrated in Figure 2(b) for several values of $E(H\alpha)$ using our grid of models. We see that for $E(H\alpha) \leqslant 10^5$, the curves are rather flat, and then for a given observed T_b one obtains nonunique solutions for T_k. Taking into account certain calibration inaccuracies, such inversion problem is ill conditioned. We thus consider only the bright pixels with $E(H\alpha) \geqslant 10^5$ cgs and
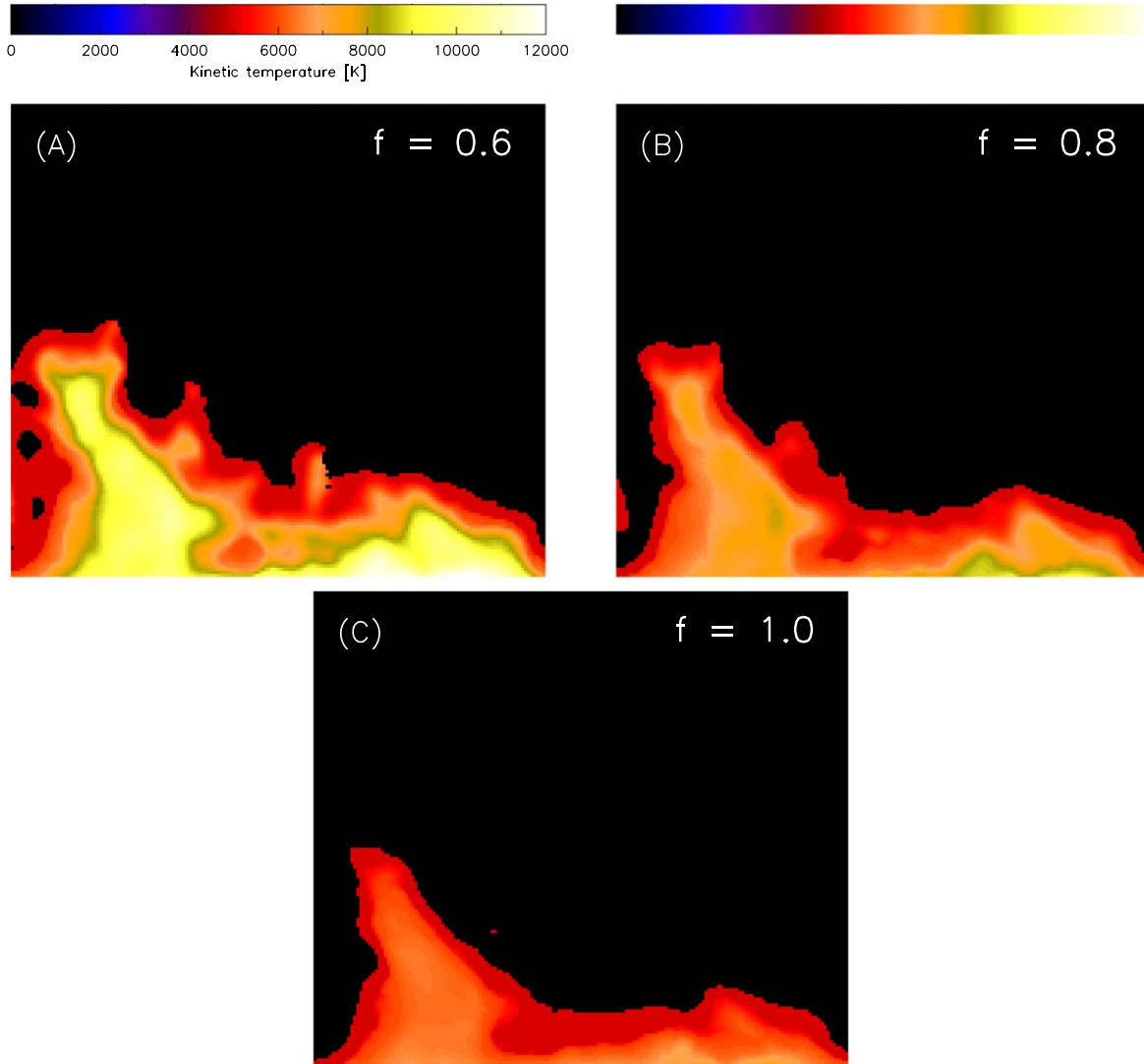
Figure 3. Inverted maps of kinetic temperatures for different values of the filling factor: (A) $f = 0.6$, (B) $f = 0.8$, and (C) $f = 1.0$. The field of view is the same as in Figure 1. A more extended prominence area at lower f is due to weaker structures in Hα taken into account—see the text.

proceed as described above up to the point when we get a variation of T_b versus T_k using the grid of models (i.e., variations like those shown in Figure 2(b)). Then we search for the best fit between these T_b and the observed one divided by the filling factor f at each pixel. Note that we apply the same filling factor also to MSDP observations, which have a similar spatial resolution to the current ALMA Band 3. We thus divide the observed $E(\mathrm{H}\alpha)$ by the same value of f. The resulting maps of the plasma kinetic temperatures are shown in Figure 3 for different values of f, which is taken to be uniform for the whole FoV. For $f = 1$ we have low observed T_b, which causes the inverted T_k to tend to reach the lowest values in the grid (down to 5000 K). On the other hand, for $f = 0.6$ the obtained T_k values may go to the upper limit of 12,000 K—we assume that the temperatures of the cool parts of the prominence do not exceed this value. Setting a higher limit would lead to nonunique inversions. From the presented maps, we conclude that a reasonable fit is obtained for f around 0.8, but of course, this is just an estimate because different parts of the prominence may have different f as seems to be the case from

Figure 2(a). The range of inverted temperatures for $f = 0.8$ looks consistent with the behavior in Figure 2(a). Note also that the inverted area somewhat expands when f decreases due to the extension of the observed $E(\mathrm{H}\alpha)$ to lower values.

Low-temperature areas around the borders of the prominence are somewhat surprising; one would expect higher temperatures at the edges. However, there are three factors that may play a role. First, these areas are in fact not real prominence edges because we limited our analysis only to the brightest parts while in Figure 1 we clearly see more extended but fainter parts. Second, the pattern in our temperature maps is certainly influenced by the assumed uniformity of the filling factor f—fainter structures may have much lower f and thus their kinetic temperature will be in fact higher. Finally, we limited our inversions by $T_k = 12,000$ K, and relaxing this, we could get two distinct solutions for T_k: one that tends toward the low temperatures (as in our maps) and the other that may have temperatures larger than 12,000 K (see Figure 2(b)). This kind of bifurcation must be constrained by other independent spectral diagnostics.

5.3. Grid of Non-LTE Models

Our extended grid of 1D slab non-LTE models constructed for this work consists of 131 temperatures covering the range from 5000 to 18,000 K with the step of 100 K; it covers a reasonable range of gas pressures from 0.01 to 1.0 dyn cm^{-2} and of effective prominence thicknesses along the LoS from 500 to 5000 km with the step of 100 km. For each temperature, we have 828 models and altogether we computed $131 \times 828 = 108,468$ models. The non-LTE models are based on the MALI technique as described in Heinzel ([1995](#)), but here we used the partial redistribution for the hydrogen Lyα and Lyβ lines. We use only one characteristic microturbulent velocity, 5 km s^{-1}, and one mean height above the limb to specify the diluted incident radiation illuminating the prominence slab on both sides. Here it is worth mentioning that although the ALMA continuum source function is Planckian (Section [4](#)), the EM, or more precisely the product of electron and proton density times the effective thickness, results from the non-LTE modeling of hydrogen ionization, which represents the very complex task undertaken here. In this work, we set $n_e = n_p$ because our radiative-transfer non-LTE code does not account for the ionization of other species and namely of helium. This is quite reasonable in cool prominence regions where helium does not contribute to the electron density more than typically 10%.

Our 1D slab models are static in this exploratory work, while the real Hα line profiles can be affected by plasma dynamics. Hydrogen lines are less sensitive to microturbulent broadening than those of other heavier species, but the line profiles are still shaped by macroscopic fine-structure motions if present, as shown, e.g., in Gunár et al. ([2012](#)). However, we assume here that observed integrated line emission is not much influenced by motions and thus that static models are adequate for this exploratory study.

### 6. Discussion and Future Prospects

The principal aim of this exploratory work was to demonstrate the ability of ALMA to provide diagnostics of the prominence kinetic temperature. Using observations currently available only in a single band at a time, we demonstrate how the temperature can be derived based on additional constraints provided by the cotemporal and cospatial Hα observations. The method described here works reasonably well for bright prominence structures, which become optically thick in Hα and also in the considered ALMA band, but for weaker features, the inversion is ill conditioned, which is even worse if the data uncertainties are considered. However, we found a high sensitivity of the results to the adopted values of the PoS filling factor, an issue to be further investigated. In fact, even for weak structures, the solution could be obtained provided that they are weak due to a very small filling factor. In our analysis we considered a uniform filling factor over the whole FoV and have shown the inversions for its different values. But in reality, weak features may be due to very small factors, while the brightest ones may have filling factors closer to unity. For future ALMA observations, it would be useful to get data in several (at least two rather distinct) bands and test such multiband diagnostics against the one developed here. We are fully aware of simplifications in our non-LTE modeling used for this work and plan to extend it to a fine-structure case including the prominence–corona transition region (PCTR) as previously done for other diagnostics. But as discussed above, the fine-structure dynamics is not affecting our results based on continuum observations, and only some marginal influence can be expected on integrated Hα emission. Full 3D modeling of ALMA visibility of heterogeneous prominences was already performed in Gunár et al. ([2016](#), [2018](#)), but the next step is to consider relevant inversion strategies. The principal conclusion here is that ALMA provides reliable data for prominence temperature diagnostics and these data give results that are consistent with the Hα observations. Our diagnostics here was shown to be limited to a certain range of Hα intensities; otherwise, the inversions are problematic. A possible solution is to add another independent diagnostic based on lines of other species like Ca II and Mg II (see e.g., the chromospheric inversions of da Silva Santos et al. [2018](#)). The ALMA community is continuously developing methods of data reduction and calibration and, specifically for off-limb targets, this represents a challenge because of the presence of sharp limbs. Contrary to previous expectations, the current ALMA Band 3 prominence observations have an order-of-magnitude lower resolution, which is comparable to Hα MSDP observations or somewhat better (see Figure [1](#)). Future prominence observations should be optimized for higher spatial resolutions and (quasi-)simultaneously in at least two distinct bands.

ORCID iDs

Petr Heinzel ⬤ https://orcid.org/0000-0002-5778-2600
Arkadiusz Berlicki ⬤ https://orcid.org/0000-0002-6505-4478
Miroslav Bárta ⬤ https://orcid.org/0000-0002-5092-9462
Paweł Rudawy ⬤ https://orcid.org/0000-0002-3898-1619
Stanislav Gunár ⬤ https://orcid.org/0000-0003-3889-2609
Nicolas Labrosse ⬤ https://orcid.org/0000-0002-4638-157X
Krzysztof Radziszewski ⬤ https://orcid.org/0000-0003-0310-1598

References

Alissandrakis, C. E., Patsourakos, S., Nindos, A., & Bastian, T. S. 2017, A&A, 605, A78

Bastian, T. S., Ewell, M. W., & Zirin, H, J. 1993, ApJ, 418, 510

da Silva Santos, J. M., de la Cruz Rodríguez, J., & Leenaarts, J. 2018, A&A, 620, A124

Gilbert, H. 2015, in Astrophysics and Space Science Library, Solar Prominences, ed. J.-C. Vial & O. Engvold, 415 (Cham: Springer), 157

Gnevyshev, M. N., Nikolsky, G. M., & Sazanov, A. A. 1967, SoPh, 2, 223

Gouttebroze, P., Heinzel, P., & Vial, J. C. 1993, A&AS, 99, 513

Gunár, S., Heinzel, P., Anzer, U., & Mackay, D. H. 2018, ApJ, 853, 21

Gunár, S., Heinzel, P., Mackay, D. H., & Anzer, U. 2016, ApJ, 833, 141

Gunár, S., Mein, P., Schmieder, B., Heinzel, P., & Mein, N. 2012, A&A, 543, A93

Heinzel, P. 1995, A&A, 299, 563

Heinzel, P., Berlicki, A., Bárta, M., Karlický, M., & Rudawy, P. 2015, SoPh, 290, 1981

Irimajiri, Y., Takano, T., Nakajima, H., et al. 1995, SoPh, 156, 363

Labrosse, N., Heinzel, P., Vial, J. C., et al. 2010, SSRv, 151, 243

Labrosse, N., Rodger, A. S., Radziszewski, K., et al. 2022, arXiv:2202.12434

Mein, P. 1977, SoPh, 54, 45

Mein, P. 1991, A&A, 248, 669

Okada, S., Ichimoto, K., Machida, A., et al. 2020, PASJ, 72, 71

Park, H., Chae, J., Song, D., et al. 2013, SoPh, 288, 105

Peat, A. W., Labrosse, N., Schmieder, B., & Barczynski, K. 2021, A&A, 653, A5

Rodger, A. 2019, PhD thesis, University of Glasgow

Rodger, A., & Labrosse, N. 2017, SoPh, 292, 130

Rompolt, B. 1994, JOSO Annual Report, 1993, 87

Rompolt, B., & Rudawy, P. 1985, PoAst, 33, 141

Ruan, G., Jejčič, S., Schmieder, B., et al. 2019, ApJ, 886, 134

Shimojo, M., Bastian, T. S., Hales, A. S., et al. 2017, SoPh, 292, 87

Skokić, I., & Brajša, R. 2019, arXiv:1904.08263

Vial, J.-C., & Engvold, O. 2015, in Astrophysics and Space Science Library, Solar Prominences, ed. J.-C. Vial & O. Engvold, 415 (Cham: Springer)

Wedemeyer, S., Bastian, T., Brajša, R., et al. 2016, SSRv, 200, 1

White, S. M., Iwai, K., Phillips, N. M., et al. 2017, SoPh, 292, 88